# Pore-Wall Chemistry and Photocatalytic Activity of Mesoporous Titania Molecular Sieve Films

Jimmy C. Yu,*,† Xinchen Wang,† and Xianzhi Fu‡

*Department of Chemistry and Environmental Science Program, The Chinese University of Hong Kong, Shatin, New Territories, Hong Kong, and Research Institute of Photocatalysis, College of Chemistry & Chemical Engineering, Fuzhou University, Fuzhou 350002, P. R. China*

*Received January 7, 2004. Revised Manuscript Received February 4, 2004*

Transparent zeolite-like mesoporous $TiO_2$ nanocrystalline thin films with high photocatalytic activity were synthesized via a surfactant-templated method. The films were characterized by TGA−DTA, XRD, nitrogen adsorption, SEM, TEM, UV/vis, and FT-IR spectroscopy. The photocatalytic activity of the films was evaluated by photodecomposition of acetone in air at ambient conditions. It was found that thermal treatment resulted in surfactant elimination, framework solidification, as well as pore-wall crystallization of the mesoporous $TiO_2$. The resulting zeolite-like mesoporous $TiO_2$ nanocrystalline films had large specific surface areas (∼100 $m^2/g$), high porosity (∼40%), extended band gap energy (∼3.3 eV), tridirectional communicating pore systems, and enhanced photocatalytic activity. The optimum calcination temperature was found to be 500 °C, at which the film possessed a cubic ordered mesoporous structure and exhibited the highest photocatalytic activity. A comparison with a conventional $TiO_2$ film (prepared from a sol−gel method) showed that the ordered mesoporous $TiO_2$ nanocrystalline film (calcined at 500 °C) had over 2 times the specific photocatalytic activity as the conventional film. The high photocatalytic activity of zeolite-like mesoporous $TiO_2$ thin films can be explained by the large specific surface area and the three-dimensionally connected mesoporous architecture.

## 1. Introduction

Since surfactant-templated silica was first synthesized in 1992 by Mobile scientists, there has been extensive research in the field, motivated by the promising applications of these zeolite-like solids in catalysis, sorption, biotechnology, and nanostructure fabrications.[1] In the original preparation, silicate species were nucleating and condensing on the surface of cationic surfactant arrays under basic environments, inducing regular mesopore ordering. This synthetic strategy is based on the well-known phenomenon of self-organization of surfactant molecules into mesophase such that the combined assembly of organic molecules acted as a template around which an inorganic material could be formed. Recently, the approach has been extended to synthesize transition-metal oxides, which have a wide domain of applications due to their special optical/electronic/magnetic properties.[2] Among these materials, titanium dioxide is of particular interest as a semiconductor photocatalyst. The semiconductor photocatalysis is initiated by the surface trapping of photogenerated electrons ($e^-$) and holes ($h^+$), which induces interfacial electron-transfer reactions with adsorbed substrates.[3] These photocatalytic processes impart a number of useful properties to the surface of $TiO_2$, making it antibacterial, antifogging, self-cleaning, and able to destroy organic pollutants.[4] To utilize these excellent properties for practical applications, processing the $TiO_2$ as immobilized coatings is required.

Titanium dioxide thin films have been extensively investigated for many years.[5] However, most of the attempts to prepare such films involved the deposition and sintering of sol−gel-driven $TiO_2$ nanoparticles. This would form aggregates of particles rather than a continuous and periodic inorganic framework. Ordered

* Corresponding author. Tel: (852) 2609 6268. Fax: (852) 2603 5057. E-mail: jimyu@cuhk.edu.hk.

† The Chinese University of Hong Kong.

‡ Fuzhou University.

(1) (a) Kresge, C. T.; Leonowicz, M. E.; Roth, W. J.; Vartuli, J. C.; Beck, J. S. *Nature* **1992**, *359*, 710. (b) Beck, J. S.; Vartuli, J. C.; Roth, W. J.; Leonowicz, M. E.; Kresge, C. T.; Schmitt, K. D.; Chu, C. T. W.; Olson, D. H.; Sheppard, E. W.; Mccullen, S. B.; Higgings, J. B.; Schlenker, J. L. *J. Am. Chem. Soc.* **1992**, *114*, 10834. (c) Soler-Illia, G. J. D.; Sanchez, C.; Lebeau, B.; Patarin, J. *Chem. Rev.* **2002**, *102*, 4093.

(2) (a) Yang, P.; Deng, T.; Zhao, D.; Feng, P.; Pine, D.; Chmelka, B. F.; Whitesides, G. M.; Stucky, G. D. *Science* **1998**, *282*, 2244. (b) Yang, P. D.; Zhao, D. Y.; Margolese, D. I.; Chmelka, B. F.; Stucky, G. D. *Nature* **1998**, *396*, 152. (c) Crepaldi, E. L.; Soler-Illia, G. J. D. A.; Bouchara, A.; Grosso, D.; Durand, D.; Sanchez, C. *Angew. Chem., Int. Ed.* **2003**, *42*, 347. (d) Mamak, M.; Coombs, N.; Ozin, G. *J. Am. Chem. Soc.* **2000**, *122*, 8932. (e) Antonelli, D. M.; Ying, J. Y. *Chem. Mater.* **1996**, *8*, 874.

(3) (a) Hoffmann, M. R.; Martin, S. T.; Choi, W.; Bahnemann, D. W. *Chem. Rev.* **1995**, *95*, 69. (b) Linsebiler, A. L.; Lu, G.; Yates, J. T. *Chem. Rev.* **1995**, *95*, 735.

(4) (a) Wang, R.; Hashimoto, K.; Fujishima, A.; Chikuni, M.; Kojima, E.; Kitamura, A.; Shimohigoshi, M.; Watanabe, T. *Nature* **1997**, *388*, 431. (b) Fujishima, A.; Hashimoto, K. *Abstr. Pap. Am. Chem.* S 211: 263-PHYS Part 2 MAR 24 **1996**. (c) Wolfrum, E. J.; Huang, J.; Blake, D. M.; Maness, P. C.; Huang, Z.; Fiest J.; Jacoby, W. A. *Environ. Sci. Technol.* **2002**, *36*, 3412. (d) Miyauchi, M.; Nakajima, A.; Hashimoto, K.; Watanabe, T. *Adv. Mater.* **2000**, *12*, 1923. (e) Nakajima, A.; Koizumi, S.; Watanabe, T.; Hashimoto, K. *Langmuir* **2000**, *16*, 7048. (f) Lu, Z.; Zhou, L.; Zhang, Z.; Shi. W.; Xie, Z.; Xie, H.; Pang, D.; Shen, P. *J. Phys. Chem. B* **2003**, *19*, 8765.

10.1021/cm049955x CCC: $27.50 
Published on Web 03/12/2004

mesoporous $TiO_2$ film can be viewed as a regular ensemble of individual $TiO_2$ nanoparticles sintered together to establish an electronic semiconducting network, inside which are periodic cavities and channels. Such a zeolite-like structural feature may have interesting bulk-chemistry applications, especially for heterogeneous photocatalysis. This is because they enhance light harvesting due to an enlarged surface area and multiple scattering, and also because they introduce continuous pore channels that facilitate the transfer of reactant molecules.[6] Moreover, the periodic surface structure allows structural orientation of guest molecules in the pores, which may result in the enhancement of activity and selectivity in catalysis.[7]

The evaporation-induced self-assembly (EISA) method initiated by Brinker and co-workers for mesoporous silica film is also effective for the preparation of highly organized mesoporous $TiO_2$ thin films.[8] In the EISA process, the evaporation of solvent (typically, ethanol) enriches the surfactant and inorganic species to form mesophases at the substrate−liquid, and liquid−air interfaces, resulting in well-defined mesostructured hybrids. Subsequent thermal treatment of the hybrids would generate ordered mesoporous silica frameworks. Stucky et al. and Sanchez et al. extended the EISA approach to prepare mesostructured $TiO_2$ and $ZrO_2$ thin films from alkoxide−alcohol−water−HCl mixtures using tribrock copolymers as the structure-directing agents.[9] They both proposed potential applications of the zeolite-like $TiO_2$ thin films in photocatalytic processes. However, to date, practical applications of the $TiO_2$ mesoporous molecular sieve films in photocatalytic fields have not been reported.

The photocatalytic activity of $TiO_2$ is strongly dependent on its pore-wall chemistry.[3] Ying et al. reported that anatase-$TiO_2$ with particle size of about 10 nm was a superior photocatalyst due to its low surface $e^-/h^+$ recombination rate.[10] Fu et al. attributed the improved photocatalytic performance of $TiO_2$–$SiO_2$ and $TiO_2$–$ZrO_2$ binary metal oxides to their large surface areas and high surface acidities.[11] Recently, we have reported the effect of thermal treatment on the surface microstructure and photocatalytic activity of nonordered $TiO_2$ thin films.[12] However, the relationships among sintering temperature, pore-wall chemistry, and photocatalytic activity of highly ordered mesoporous $TiO_2$ thin films have not been documented.

In this study, we present the synthesis, characterization, and photocatalytic activity of highly ordered mesoporous $TiO_2$ thin films prepared by the EISA method. Our primary interest is the effect of sintering temperature on the pore-wall chemistry and photocatalytic performance. Results show that well-ordered mesoporous structures with crystalline frameworks can be obtained by controlling the sintering temperature. These zeolite-like mesoporous anatase-$TiO_2$ thin films have large surface areas and are photocatalytically more active than conventional $TiO_2$ films.

## 2. Experimental Section

**2.1. Preparation.** Titanium tetraisopropoxide (TTIP) (Aldrich) was used as the inorganic source. Poly(ethylene oxide)-based triblock copolymer $[HO(CH_2CH_2O)_n-(CH_2CH(CH_3)O)_m-(CH_2CH_2O)_nH]$, Pluronic P123 (P123, average $n/m$ = 20/70, MW = 5800) was used as the structural-directing agent. The template is commercially available from Aldrich.

In a typical synthesis, a solution of TTIP in concentrated HCl (37%) was added dropwise into an ethanolic solution of the template in the molar ratio 1:15:0.01:1.6:5.4 TTIP:ethanol:P123:HCl:$H_2O$. The resulting $TiO_2$ sol solution was vigorously stirred for 5 min at room temperature and then aged at 4 °C for 10 min. The cooled stock sol solution was used for dip-coating glass substrates, quartz slides, or silicon wafers at a constant withdraw rate of 10 cm/min. The as-prepared thin films were aged at 4 °C for 24 h and 25 °C for 1 h continuously. The films were subsequently treated with $NH_3$ vapor for 5 s. After that, the films were heated at 60, 80, 120, and 200 °C for 12 h, respectively. Calcinations were done in static air at 300−600 °C for 4 h (ramp of 1 °C $min^{-1}$). This resulted in continuous, transparent films with ∼0.4 $\mu$m thickness as measured by a α-step profilometer. The thickness of the films could be easily controlled by dip-coating cycles or by using sol solutions with different concentrations. As distinct from the methods proposed by Stucky and Sanchez, the mother sol and as-prepared films were aged at the lower temperature of 4 °C in our preparation. The low temperature is favorable for the formation of cubic phase in the binary water−P123 system at higher block copolymer concentrations.[13]

**2.2. Characterization.** Simultaneous thermogravimetric analyses (TGA) and differential thermal analyses (DTA) were performed on a Setaram TGA−DTA 92-16 thermal analysis instrument. Measurements were taken with a heating rate of 5 °C/min from 30 to 800 °C. Low-angle X-ray diffraction (XRD) diagrams were collected in $\theta-2\theta$ mode using a Bruker D8 Advance X-ray diffractometer (Cu K$\alpha_1$ irradiation, $\lambda$ = 1.5406 Å). Wide-angle XRD patterns were collected in a parallel mode ($\omega$ = 0.5°, $2\theta$ varied from 20° to 60°, Cu K$\alpha_1$ irradiation) using a Bruker D8 Advance X-ray diffractometer with a thin film optic. The crystal size was estimated by applying the Scherrer equation to the fwhm of the (101) peak of anatase-$TiO_2$, with silicon as a standard of the instrumental line broadening. Scanning electron microscopy (SEM) was taken on a LEO 1450VP scanning microscope to investigate the surface roughness and morphology of the films. Transmission electron microscopy (TEM) and high-resolution transmission electron microscopy (HRTEM) were recorded on a JEOL 2010F micro-

(5) (a) Negishi, N.; Iyoda, T.; Hashimoto, H.; Fujishima, A. *Chem. Lett.* **1995**, 841. (b) Stathatos, E.; Lianos, P.; DelMonte, F.; Levy, D.; Tsiourvas, D. *J. Sol−Gel Technol.* **1997**, *10*, 83. (c) Bilmes, S. A.; Mandelbaum, P.; Alvarez, F.; Victoria, N. M. *J. Phys. Chem. B* **2000**, *104*, 9851. (d) Huang, J.; Ichinose, I.; Kunitake, T.; Nakao, A. *Langmuir* **2002**, *18*, 9048. (e) Zhang, L.; Zhu, Y. F.; He, Y.; Li, W.; Sun, H. B. *Appl. Catal. B-Environ.* **2003**, *40*, 287. (f) Yu, J. C.; Ho, W. K.; Yu, J. G.; Hark, S. K.; Iu, K. *Langmuir* **2003**, *19*, 3889.

(6) (a) Hagfeldt, A.; Grätzel, M. *Acc. Chem. Res.* **2000**, *33*, 269. (b) Rolison, D. R. *Science* **2003**, *14*, 1698.

(7) (a) Yang, Q. H.; Kapoor, M. P.; Inagaki, S. *J. Am. Chem. Soc.* **2002**, *124*, 9694. (b) Stein, A.; Melde, B. J.; Schroden, R. C. *Adv. Mater.* **2002**, *12*, 1403.

(8) (a) Lu, Y. F.; Ganguli, R.; Drewien, C. A.; Anderson, M. T.; Brinker, C. J.; Gong, W. L.; Guo, Y. X.; Soyez, H.; Dunn, B.; Huang, M. H.; Zink, J. I. *Nature* **1997**, *389*, 364. (b) Brinker, C. J.; Lu, Y. F.; Sellinger, A.; Fan, H. Y. *Adv. Mater.* **1999**, *11*, 579. (c) Gibaud, A.; Grosso, D.; Smarsly, B.; Baptiste, A.; Bardeau, J. F.; Babonneau, F.; Doshi, D. A.; Chen, Z.; Brinker, C. J.; Sanchez, C. *J. Phys. Chem. B* **2003**, *107*, 6114.

(9) (a) Alberius, C. A.; Frindell, K. L.; Hayward, R. C.; Kramer, E. J.; Stucky, G. D.; Chmelka, B. F. *Chem. Mater.* **2002**, *14*, 3284. (b) Crepaidi, E. L.; Soler-lllia, G. J. de A. A.; Grosso, D.; Cagnol, F.; Ribot, F.; Sanchez, C. *J. Am. Chem. Soc.* **2003**, *125*, 9770. (c) Crepaidi, E. L.; Soler-lllia, G. J. de A. A.; Grosso, D.; Sanchez, C. *New J. Chem.* **2003**, *27*, 9.

(10) (a) Zhang, Z. B.; Wang, C. C.; Zakaria, R.; Ying, J. Y. *J. Phys. Chem. B* **1998**, *102*, 10871. (b) Wang, C. C.; Zhang, Z.; Ying, J. Y. *Nanostr. Mater.* **1997**, *9*, 583.

(11) Fu, X. Z.; Clark, L. A.; Yang, Q.; Anderson, M. A. *Environ. Sci. Technol.* **1996**, *30*, 647.

(12) Yu, J. C.; Yu, J. G.; Zhao, J. C. *Appl. Catal. B-Environ.* **2002**, *36*, 31. (b) Yu, J. G.; Yu, J. C.; Ho, W. K.; Jiang, Z. T. *New J. Chem.* **2002**, *26*, 607.

(13) Wanka, G.; Hoffmann, H.; Ulvrich, W. *Macromelecules* **1994**, *27*, 4145−4149.

scope to elucidate the mesostructure of the films. Samples obtained by scratching the films from the substrates were suspended in menthol, followed by sonication for 5 min. Carbon-coated copper grids were used as the sample holders. Nitrogen adsorption−desorption isothermals were collected at 77 K using Micromeritics ASAP 2010 equipment (BET and BJH models, respectively, for specific surface area and porosity evaluation) for samples scratched off the substrate. All the samples were degassed at 120 °C and $10^{-6}$ Torr prior to the measurement. A Varian Cary 100 Scan UV/visible system was used to obtain the absorption spectra of the catalysts over a range of 200−800 nm. FT-IR spectra on pellets of the samples mixed with KBr were recorded on a Nicolet Magna 560 FT-IR spectrometer at a resolution of 4 $cm^{-1}$. The concentrations of the samples were kept around 0.25−0.3%.

**2.3. Photocatalytic Activity Measurements.** Acetone ($CH_3COCH_3$) is a common chemical that is used extensively in a variety of industrial and domestic applications. Therefore, we chose it as a model contaminant. Photocatalytic oxidation of acetone is based on the following reaction:[12]

$$CH_3COCH_3 + 4O_2 \rightarrow 3CO_2 + 3H_2O \quad (1)$$

The photocatalytic activity of the $TiO_2$ thin films toward oxidizing acetone in air was measured at ambient temperature using a 7000-mL reactor. The reactor was connected to a dryer containing $CaCl_2$ that was used for controlling the initial humidity in the reactor. The films were put into the reactor, followed by the injection of a small amount of acetone (∼25 mL) into the reactor. The acetone vapor was allowed to reach adsorption equilibrium with the films in the reactor prior to each experiment. The concentrations of acetone, carbon dioxide, and water vapor in the reactor were measured with a Photoacoustic IR Multigas Monitor (INNOVA Air Tech Instruments Model 1312). The initial concentration of acetone after the adsorption equilibrium was about 400 ± 2 ppm, which remained constant until a 15-W 365-nm UV lamp (Cole-Parmer Instrument Co.) was switched on. The initial concentration of water vapor and temperature were 1.20 ± 0.01 vol % and 25 ± 1 °C, respectively. During the photocatalytic reaction, a near 3:1 ratio of carbon dioxide products to acetone destroyed was observed, and the concentration of acetone decreased steadily with increase in UV illumination time. Each reaction was followed for 60 min. The measurements were repeated for each catalytic system, and the experimental error was found to be within ±5%.

The photocatalytic activity of the films can be quantitatively evaluated by comparing the apparent reaction rate constants. The photocatalytic degradation generally follows a Langmuir−Hinshelwood mechanism[12a,12b] with the rate $r$ being proportional to the coverage $\theta$

$$r = k\theta = kKc/(1 + Kc_o) \quad (2)$$

where $k$ is the true rate constant, which includes various parameters such as the mass of catalyst, the intensity of light, etc., and $K$ is the adsorption constant. Since the initial concentration is low ($c_o$ = 400 ppm = 4.29 × $10^{-5}$ mol/L), the term $Kc$ in the denominator can be neglected with respect to unity. The rate becomes, apparently, first order

$$r = -dc/dt = kKc = k_a c \quad (3)$$

where $k_a$ is the apparent pseudo-first-order rate constant. The integral form $c = f(t)$of the rate equation is

$$\ln(c_o/c) = k_a t \quad (4)$$

## 3. Results and Discussion

**3.1. TG−DTA Investigation.** To evaluate the effect of sintering temperature on the pore-wall properties of the P123-templated $TiO_2$ thin films, thermogravimetric analysis (TGA) and differential thermal analysis (DTA)

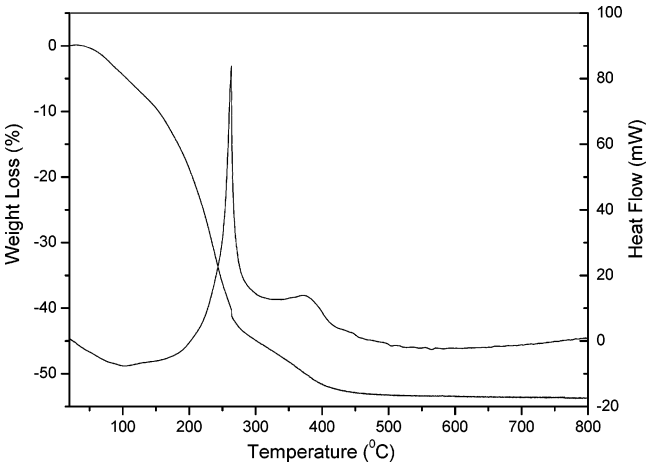


**Figure 1.** TGA−DTA curves of as-synthesized $TiO_2$ hybrid thin film templated from triblock copolymer P123.

were performed on the as-synthesized $TiO_2$ films. This study could determine the calcination temperatures at which the template and the inorganic phase began to be removed and crystallized. The TGA−DTA analysis results are shown in Figure 1. The left curve in Figure 1 represents the TGA data and the right curve the DTA results. There are three features in the DTA curve. At approximately 120 °C, a small endothermic peak is observed. This peak comes from the removal of residual and adsorbed water. An obvious exothermic peak occurs between 200 and 300 °C, which is in the range of the significant weight loss. This exothermic peak is attributed to the decomposition of the block copolymer species. The third exothermic peak at approximately 380 °C is due to the amorphous−anatase transition of $TiO_2$. In the region of 50−200 °C, the TGA curve shows a decrease in mass of ∼20%, which likely corresponds to the loss of water and HCl. The removal of the $EO_{20}PO_{70}EO_{20}$ around 200−300 °C is accompanied by another decrease in the TGA curve of ∼20%. These results prove that most of the organic template is removable from the films upon calcination at 300 °C, which is in good agreement with results reported in the literature.[9a,14]

**3.2. XRD and $N_2$-Sorption Measurements.** Figure 2 presents the low-angle X-ray diffraction (LXRD) patterns for the $TiO_2$ films. LXRD shows a gradual reduction of $d_{200}$ and a decrease in the peak intensity for treatment between 300 and 600 °C. The intense and sharp peak (fwhm = 0.062) for the 300 °C-calcined sample suggests a highly organized mesostructure in the film. These, along with the TEM results, suggest that the mesostructure belongs to a $Im\bar{3}m$ space group with a unit cell parameter of 12 nm. This is consistent with the results reported by Stucky and co-workers.[9a] The LXRD patterns of the samples are dominated by the (200) reflections, while (110) and (111) reflections have disappeared. These observations indicate that the films have an orientationally ordered 3D structure with {100} lattice planes parallel to the substrates. Similar results have also been found in block copolymer-templated silica/titania thin films.[9a,15] At 500 °C, a marked decrease in intensity and a broadening of the (200) peak

(14) Yun, H. S.; Miyazawa, K.; Zhou, H. S.; Honma, I.; Kuwabara, M. *Adv. Mater.* **2001**, *13*, 1377.
(15) Zhao, D.; Yang, P.; Melosh, N.; Feng, J.; Chemlka, B. F.; Stucky, G. D. *Adv. Mater.* **1998**, *10*, 1380.

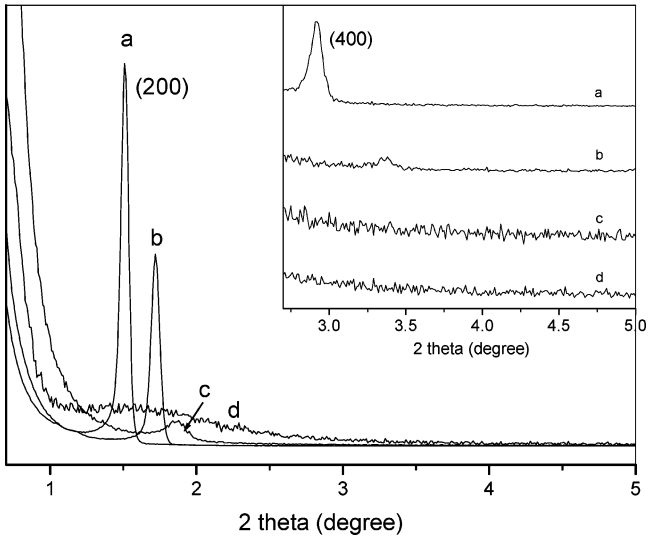


**Figure 2.** Low-angle XRD patterns of mesoporous $TiO_2$ thin films sintered at (a) 300, (b) 400, (c) 500, and (d) 600 °C.

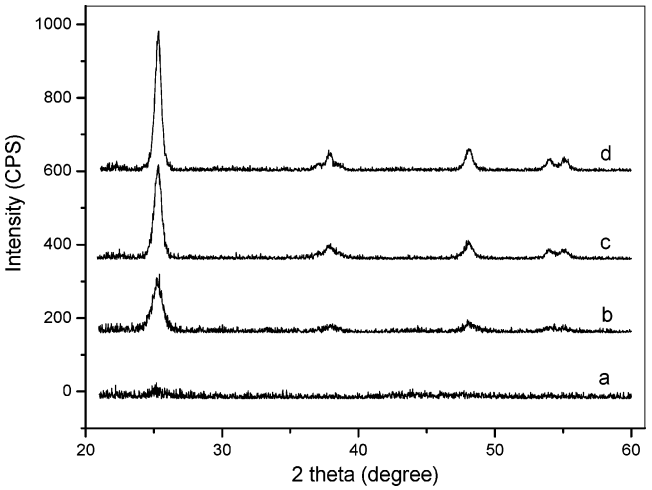


**Figure 3.** Wide-angle XRD patterns of mesoporous $TiO_2$ thin films sintered at (a) 300, (b) 400, (c) 500, and (d) 600 °C.

(fwhm = 0.136) occurs, accompanied by the disappearance of the (400) peak (Figure 2, inset). This is a reflection of a partial degradation of the ordered mesoporous structure in the film. Upon heating at 600 °C, the (200) peak was dramatically weakened and broadened (fwhm = 0.709), indicating the collapse of the mesoporous framework.

Wide-angle XRD in Figure 3 shows a gradual increasing and narrowing in the anatase-$TiO_2$ (101) peaks ($2\theta$ = 25.4°) with increasing calcination temperature. This is due to the amorphous−anatase $TiO_2$ transition and the subsequent growth of anatase-$TiO_2$ particles. At 300 °C, the film is typically XRD-amorphous. The amorphous $TiO_2$ is converted to anatase-$TiO_2$ at around 400 °C (Figure 3b), which is consistent with the TGA−DTA results. The amorphous−anatase transition and crystallite growth were accelerated by sintering the films at higher temperatures of 500 and 600 °C, as indicated by the increasing and sharpening of the (101) peaks (Figure 3c,d). The average particle size estimated from the Scherrer equation is 6.1 nm for the film sintered at 400 °C, and this increases to 8.5 and 15.3 nm at 500 and 600 °C, respectively. The well-resolved WXRD peaks corresponding to the nanoanatase-$TiO_2$ indicate

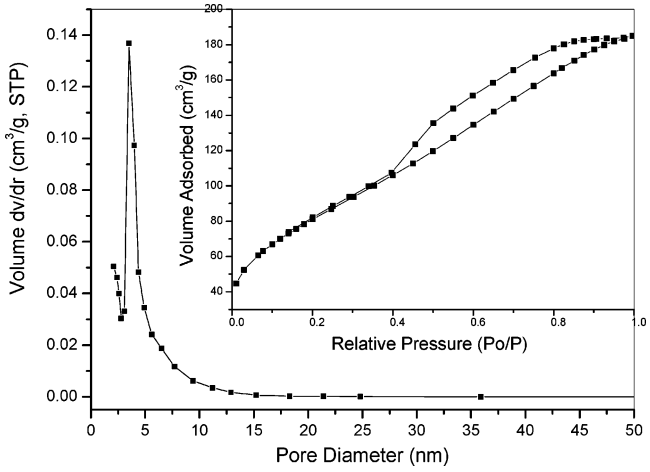


**Figure 4.** $N_2$ adsorption−desorption isothermal (inset) and corresponding BJH pore-size distribution curve of a 300 °C-sintered $TiO_2$ sample. The pore-size distribution was determined from the desorption branch of the isothermal.

the highly crystalline nature of the mesoporous framework.[16] The crystallization of the inorganic frameworks in mesoporous $TiO_2$ thin films is particularly important for their application in devices that utilize their semiconducting properties, such as photocatalysis.

We measured the BET surface areas of the samples by preparing the films with 20 coating cycles. The amount of the sample thus obtained was around 100 mg. Figure 4 shows the Barrett−Joyner−Halenda (BJH) pore size distribution plots for $N_2$-sorption isothermals for the mesoporous sample calcined at 300 °C for 4 h. The isotherms reveal stepwise adsorption and desorption, indicative of 3D intersection of a solid porous structure.[17] The BJH analyses show that the 300 °C-calcined sample exhibits a mean pore diameter ($D_{BJH}$) of 3.5 nm with a narrow distribution (fwhm = 1 nm). The wall thickness (WT) of the film, calculated from the formula WT = unit cell − $D_{BJH}$, is 8.5 nm. Such a thick inorganic wall partially explains the thermal stability (>400 °C) of the films. The BET surface area and pore-wall parameters of the mesoporous films calcined at different temperatures are summarized in Table 1. The films possess high specific surface areas and pore volumes of 299 $m^2/g$ and 0.32 $cm^3/g$, respectively, after sintering at 300 °C. Such high surface area and pore volume are partially due to the zeolite-like mesoporous structure of the films and partially due to the presence of microporosity, as evidenced by the volume adsorbed at low pressure (Figure 4). The microporosity is believed to be related to the presence of the organic impurities that causes incomplete condensation of the inorganic framework. At elevated temperatures, the specific surface areas and pore volumes decrease gradually, indicating a gradual solidification of the mesoporous framework. The $N_2$-sorption isotherms for the samples sintered at 400 and 500 °C (Supporting Information) show a decrease in volume adsorbed at low pressure, indicative of the loss of microporosity in the framework. Further increase in sintering temperature to 600 °C would

(16) Crepaldi, E. L.; Soler-Illia, G. J. D. A.; Grosso, D.; Sanchez, C. *New J. Chem.* **2003**, *27*, 9.

(17) (a) Gregg, S. J.; Sing, K. S. W. *Adsorption, Surface Area and Porosity*, Academic: London, 1997; pp 111−194. (b) Lee, B.; Lu, D.; Kondo, J. N.; Domen, K. *J. Am. Chem. Soc.* **2002**, *124*, 11256.

**Table 1. Effect of Sintering Temperature on the Pore-Wall Properties Obtained from $N_2$-Sorption and XRD Results of the Mesoporous $TiO_2$ Thin Films**

| sample | crystal phase | $S_{BET}$[a] ($m^2$/g) | $V$[b] ($cm^3$/g) | $D_{BJH}$[c] (nm) | porosity[d] (%) | fwhm ($2\theta$°) | crystal size (nm) |
|---|---|---|---|---|---|---|---|
| MT300 | amorphous[e] | 299 | 0.32 | 3.5 | 51.5 | 0.062 | 2.5[f] |
| MT400 | anatase | 113 | 0.23 | 4.6 | 46.0 | 0.068 | 6.1 |
| MT500 | anatase | 85 | 0.16 | 6.3 | 37.3 | 0.136 | 8.5 |
| MT600 | anatase | 40 | 0.11 | 8.6 | 29.2 | 0.709 | 15.4 |

[a] BET surface area calculated from the linear part of the BET plot ($P/P_0 = 0.1-0.2$). [b] Total pore volume, taken from the volume of $N_2$ adsorbed at $P/P_0 = 0.995$. [c] Average pore diameter, estimated using the desorption branch of the isotherm and the Barrett−Joyner−Halenda (BJH) formula. [d] The porosity was estimated from the pore volume determined using the desorption branch of the $N_2$ isotherm curve at $P/P_0 = 0.995$. [e] the sample was XRD-amorphous. [f] The size was estimated from an HRTEM image.

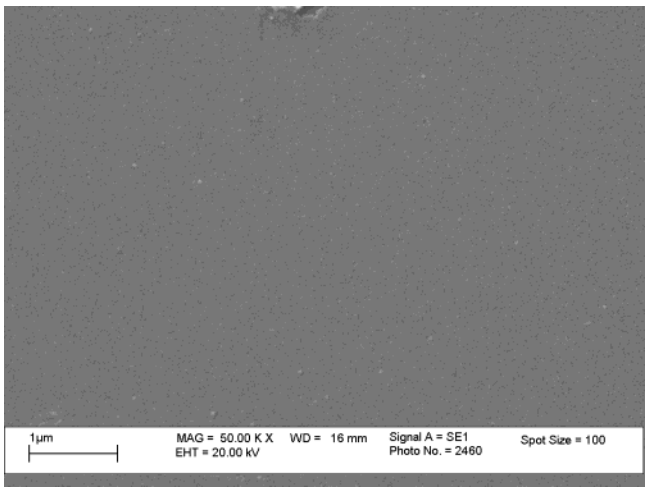


**Figure 5.** Representative SEM image of the mesoporous $TiO_2$ thin film showing a crack-free and homogeneous surface.

destroy the mesostructure. As expected, the pore volume and porosity of the samples decrease significantly at 600 °C (Table 1), and the pore size distribution becomes much broader (Supporting Information).

**3.3. SEM and TEM Studies.** The surface roughness, morphology, and mesostructure of the films were studied by scanning electron microscopy (SEM) and transition electron microscopy (TEM). In Figure 5, the SEM observation shows a glasslike surface without any structure, as expected since the particle size is typically lower than 20 nm. The glasslike coatings are crack-free and homogeneous with little surface roughness (Supporting Information). These results indicate that the thermal treatment has little effect on the macroscopic scale properties of the films. Moreover, the glasslike nature of the films suggests that the mesoporosity arises from zeolite-like structural features rather than from textural features.

To directly observe the changes of mesoporous structures during the thermal treatment process, TEM measurements were performed on the $TiO_2$ thin films. Figures 6a shows the TEM images, with different zone axes, of the $TiO_2$ film annealed at 300 °C. The 300 °C-annealing film has a long-range, cubic ordered mesostructure with a unit cell parameter of 11.8 nm, which is consistent with the results obtained by LXRD (Figure 2a). The corresponding HRTEM image shows the presence of small crystallites (<3 nm) embedded in the amorphous matrix (Figure 6b). However, no peaks for the crystalline phases could be found on their WXRD patterns (Figure 3a), apparently because both the size and the amount of crystallites were too small. Further TEM observations were carried out for mesoporous $TiO_2$ films calcined at higher temperatures, as shown in parts c and e of Figure 6 for 500 and 600 °C, respectively. At 500 °C, the cubic mesoporous structure was mostly preserved (the arrows in Figure 6c show some structural imperfections). Additionally, the coexistence of (111) and (100) lattice planes in Figure 6c indicates the loss of the highly oriented structure of the film on the substrate. These temperature-induced mesostructural changes cause a decrease and broadening of the LXRD reflections (Figure 3c). The HRTEM image of a 500 °C-calcined film also shows the existence of anatase-$TiO_2$ nanocrystals with sizes of around 8 nm (Figure 6d). It should be noted that the electron diffraction pattern of the selected area shows several weak Debye−Scherrer rings (Figure 6d, inset), corresponding to reflections of the $TiO_2$ anatase phase. These rings are absent in the 300 °C-calcined $TiO_2$ film, which may be attributed to its poor crystallization nature. When the calcination temperature is increased to 600 °C, the ordered mesostructure completely disappears in the film, as shown in Figure 6e. Meanwhile, the crystallites of about 15.3 nm are observed by XRD (Figure 3d). HRTEM shows that, at this temperature, a highly crystallized inorganic framework is formed. In fact, by changing the focus in the same region, we could observe that the lattice fringes are present throughout the structure. This extensive crystallization and crystal growth causes the collapse of the mesoporous framework, leading to the loss of surface area (Table 1) and structural ordering (Figures 2d and 6e).

**3.4. UV/Vis and FT-IR Spectrum.** Figure 7 shows the UV/visible spectra of the $TiO_2$ thin films sintered at 300, 400, 500, and 600 °C. All four samples have high transmittance of >80% over the whole visible-light region. The broad and weak absorption bands are caused by interference colors that arise as a result of the thickness of the films. The fast decay below 380 nm is due to the absorption of light caused by the excitation of electrons from the valence band to the conduction band of $TiO_2$. It is worth mentioning that the absorption edge wavelength of mesoporous $TiO_2$ thin films show a gradual pseudo-"red shift" with increasing temperatures. This is ascribed to the gradual growth of anatase-$TiO_2$ crystallites during thermal treatment from 300 to 600 °C, as confirmed by the XRD and TEM results (Table 1). The differences in absorption edge wavelength for the $TiO_2$ thin films clearly indicate a decrease in the band gap of $TiO_2$ with increasing heat treatment temperature. The band gap energies estimated from the $(ah\nu)^{1/2}$ versus photon energy plots are 3.39, 3.33, 3.27, and 3.20 eV for the $TiO_2$ films sintered at 300, 400, 500, and 600 °C, respectively.

The FT-IR spectra of the $TiO_2$ thin films sintered at different temperatures are shown in Figure 8. It is believed that the broad peak at 3400 and the peak at 1650 $cm^{-1}$ correspond to the surface-adsorbed water and hydroxyl groups. Obviously, the FT-IR measurements indicate that the surface-adsorbed water and hydroxyl group bands diminished with increasing sintering temperatures and nearly disappear at 600 °C. Small ab-

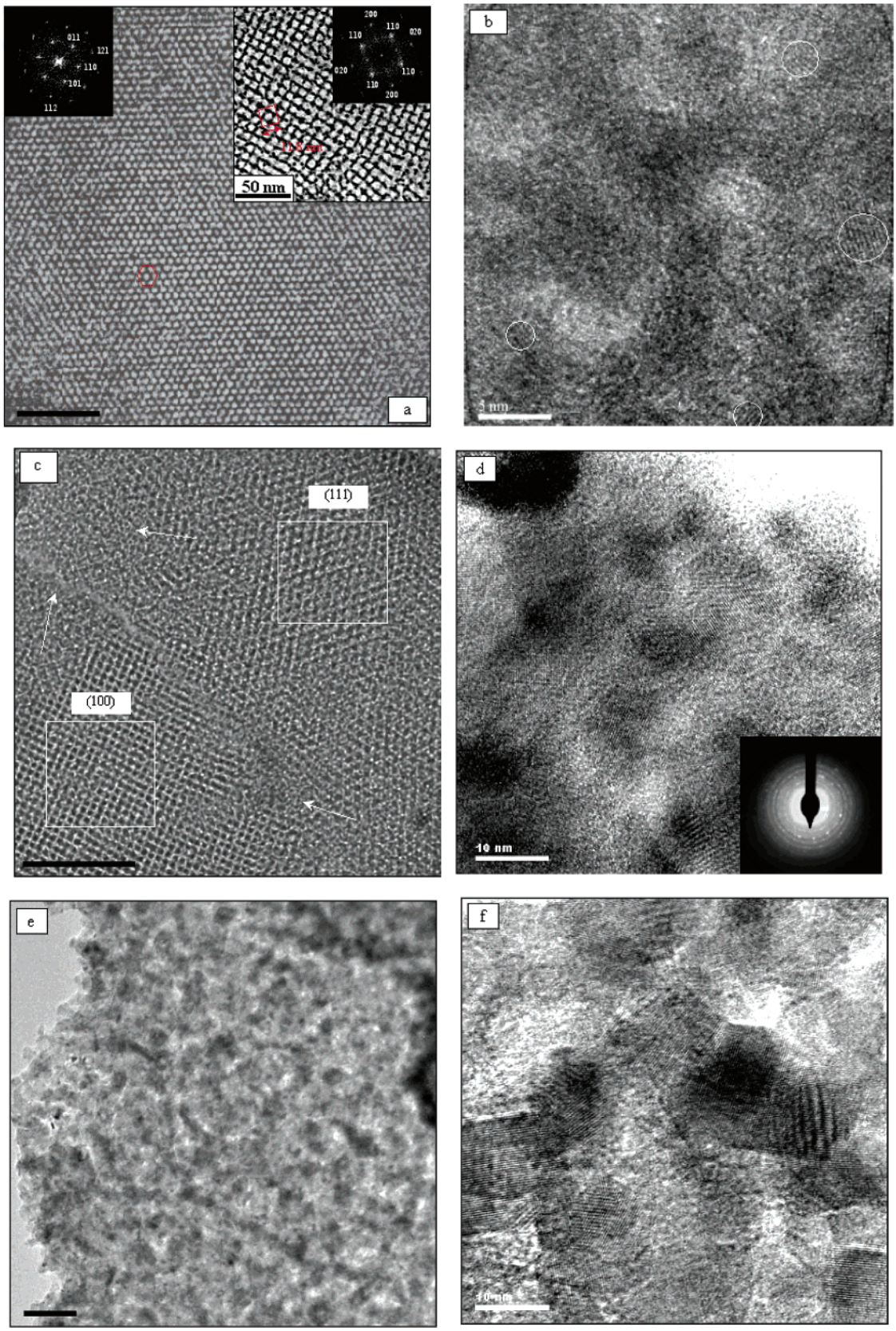


**Figure 6.** TEM and high-resolution TEM images of the mesoporous $TiO_2$ thin films sintered at (a, b) 300, (c, d) 500, and (e, f) 600 °C. The TEM image of (a) is a cross section perpendicular to the (111) direction. The left inset in part a is its Fourier transform. The right inset in a is a TEM image that is a cross section perpendicular to the (100) direction with the corresponding Fourier transform of the full image. Scale bars in parts a, c and e are 100 nm.

sorption peaks (1520 and 1432 $cm^{-1}$) corresponding to C−H vibrations in hydrocarbons[18] are observed in the film calcined at 300 °C. This is an indication of the presence of organic impurities arising from the insufficient decomposition of P123. The C−H vibrations disappear at temperatures above 400 °C, showing the

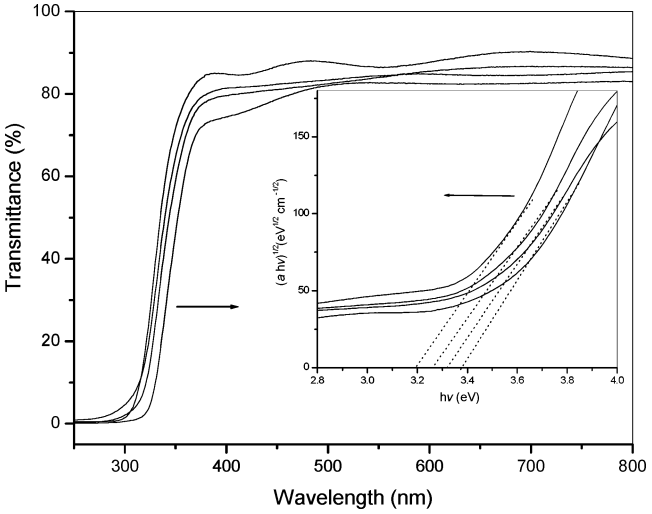


**Figure 7.** UV/vis absorption spectra of the $TiO_2$ thin films sintered at different temperatures. The inset is plots of $(ah\nu)^{1/2}$ versus photon energy, where $a$ is the absorption coefficient. Arrow direction: MT300, MT400, MT500, and MT600.

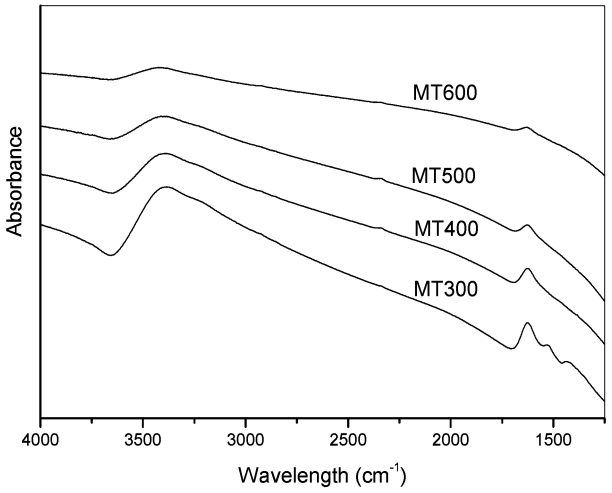


**Figure 8.** FT-IR spectra of the mesoporous $TiO_2$ thin films sintered at different temperatures.

complete removal of the P123 at high calcination temperatures. These results are in good accordance with the TGA−DTA analysis.

**3.5. Photocatalytic Activity.** Table 2 shows the activity of mesoporous $TiO_2$ thin films calcined at 300, 400, 500, and 600 °C. As expected, the sintering temperature affects the photocatalytic activity of $TiO_2$ films toward oxidizing acetone in air. The activities of the mesoporous $TiO_2$ films is initially quite low and increased quickly with increasing sintering temperature up to 500 °C. The increased activities can be attributed to the gradual crystallization of the pore-wall frameworks with increasing sintering temperature. At 300 °C, the $TiO_2$ film is typically XRD-amorphous, which has long been considered as the less photocatalytically active form of titania.[19] With increasing sintering temperature up to 500 °C, this amorphous-$TiO_2$ is gradually converted to the highly active anantase-$TiO_2$ nanocrystals. The poor photocatalytic activity of the $TiO_2$ films

**Table 2. Photocatalytic Activity of Mesoporous $TiO_2$ Thin Films Sintered at Different Temperatures and Their Comparison with a Conventional $TiO_2$ Thin Film[a]**

| sample | mass (mg) | degradation[b] rate (%) | rate constant, $K$ ($min^{-1}$) | specific photoactivity (mol $g^{-1}$ $h^{-1}$)[c] | specific photoactivity (mol $m^{-2}$ $h^{-1}$)[d] |
|---|---|---|---|---|---|
| MT300 | 13.2 | 1.6 | $2.6 \times 10^{-4}$ | $4.0 \times 10^{-4}$ | $3.8 \times 10^{-4}$ |
| MT400 | 12.5 | 9.9 | $16.4 \times 10^{-4}$ | $2.6 \times 10^{-3}$ | $2.3 \times 10^{-3}$ |
| MT500 | 12.2 | 11.6 | $19.4 \times 10^{-4}$ | $3.1 \times 10^{-3}$ | $2.7 \times 10^{-3}$ |
| MT600 | 11.8 | 7.9 | $10.8 \times 10^{-4}$ | $1.8 \times 10^{-3}$ | $1.5 \times 10^{-3}$ |
| $TiO_2$-500[e] | 8.8 | 4.8 | $7.6 \times 10^{-4}$ | $1.9 \times 10^{-3}$ | $1.2 \times 10^{-3}$ |

[a] The area of the substrates covered by the $TiO_2$ monolayer was 140 $cm^2$. [b] Average degradation rate of acetone after 1 h of photocatalytic reaction. [c] Acetone degradation amount per unit mass catalyst after 1 h of photocatalytic reaction. [d] Acetone degradation amount per unit film surface after 1 h of photocatalytic reaction. [e] Data from Table 5 of ref 12a.

calcined at 600 °C can be explained by the band gap energy, the surface properties, as well as the mesoporous architecture.

It is commonly accepted that a larger band gap energy corresponds to a more powerful redox capability. Since the 500 °C-calcined film has a larger band gap than the 600 °C-calcined film, its oxidizing ability should be stronger. Moreover, the oxidative reaction of acetone is believed to be initiated by •OH radicals. In the presence of $O_2$, the •OH radicals are generated in the following photochemical reactions:[20]

$$TiO_2 \rightarrow h^+ + e^- \quad (5)$$

$$e^- + O_2 \rightarrow O_2^- \quad (6)$$

$$O_2^- + 2H^+ + e^- \rightarrow H_2O_2 \quad (7)$$

$$H_2O_2 + O_2^- \rightarrow \bullet OH + OH^- + O_2 \quad (8)$$

$$h^+ + H_2O \rightarrow \bullet OH + H^+ \quad (9)$$

$$h^+ + OH^- \rightarrow \bullet OH \quad (10)$$

The 500 °C-calcined film possesses a higher surface area than the 600 °C-calcined film. Mesoporous $TiO_2$ films of larger surface can offer more active sites to adsorb water and hydroxyl group. According to eqs 9 and 10, the surface-adsorbed water and hydroxyl groups capture holes generated by illumination and produce active hydroxyl radicals, which are powerful oxidants in oxidizing adsorbed molecules. The capturing of holes can also inhabit the electron−hole pair recombination and, therefore, increase quantum yield.[3] Thus, a greater number of surface-adsorbed water and hydroxyl groups yields a higher reaction rate. In fact, such a relationship has been observed previously.[21]

Furthermore, the cubic ordered mesoporous architecture may also contribute to the high photocatalytic activity of the film calcinated at 500 °C. It was noted that chemical reactions are most effective when the transport paths through which molecules move into or out of the nanostructured materials are included as an

(18) Silverstein, R. M.; Bassler, G. C. *Spectrometric Identification of Organic Compounds*, John Wiley & Sons: New York, 1967.
(19) Ohtani, B.; Ogawa, Y.; Nishimoto, S. I. *J. Phys. Chem.* B **1997**, *101*, 3746.
(20) Yamashita, H.; Honda, M.; Harada, M.; Ichihashi, Y.; Anpo, M.; Hirao, T.; Itoh, N.; Iwamoto, N. *J. Phys. Chem.* B. **1998**, *102*, 10707.
(21) (a) Oosawa, Y.; Grätzel, M. *J. Chem. Soc., Faraday Trans. 1* **1988**, *84*, 197. (b) Kobayakawa, K.; Nakazawa, Y.; Sato, Y. Fujishima, A. Ber. Bunsen-ges. *Phys. Chem.* **1990**, *94*, 1439. (c) Yu, J. C.; Zhang, L. Z.; Zheng, Z.; Zhao, J. C. *Chem. Mater.* **2003**, *15*, 2280.

**Scheme 1. Three-Dimensional Mesoporous Architecture in the $TiO_2$ Nanocrystalline Thin Film with Continuous and Periodically Porous Networks That Offer Transport Routes for Gaseous Reactants to Move into and out of the Framework**

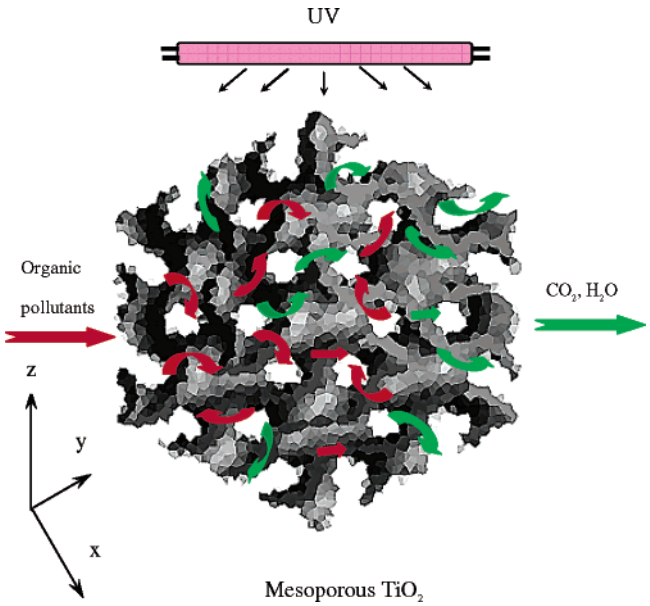


integral part of the architectural design.[22] The three-dimensionally interconnected mesochannels in the cubic mesoporous $TiO_2$ thin film serve as efficient transport paths for gaseous reactants and products in photocatalytic reactions, as elucidated in Scheme 1. When the cubic ordered mesoporous $TiO_2$ nanocrystalline thin film was illuminated by near-UV, it initiated a series of chemical reactions to generate a strong oxidizing environment on the film. This photocatalytically active film can cause breakdown of organic pollutants into nontoxic $CO_2$ and $H_2O$. The regular mesoporous channels located throughout the film allow the effective transportation of organic pollutants (i.e., acetone) to photocatalytic active sizes on the $TiO_2$ framework walls and conversely the fast diffusion of the $CO_2$ product. Since the mesoporous channels are better preserved in the 500 °C-sintering $TiO_2$ film than in the 600 °C-sintering film, the former possessed higher photocatalytic reactivity. The beneficial effect of the three-dimensional mesoporous architecture with continuous porous networks on conventional catalysis has been reported.[23] However, to the best of our knowledge, this is the first evidence of a similar effect in heterogeneous photocatalytic reactions.

A comparison between the photocatalytic activities of the mesoporous $TiO_2$ films and a conventional $TiO_2$ film synthesized from a sol−gel approach is also shown in Table 2. It is obvious that the photocatalytic activities of the mesoporous $TiO_2$ film (calcined at 500 °C) are much higher than that of the conventional $TiO_2$ film. This is probably due to the large BET specific surface area as well as the highly organized mesostructure of the P123-templated $TiO_2$ film. The specific surface area of mesoporous $TiO_2$ can be as high as 85 $m^2/g$, while that of the sol−gel-driven $TiO_2$ (typically nonporous structure) is only 9.1 $m^2/g$.[12a]

## 4. Conclusions

Crack-free, homogeneous, transparent, mesoporous $TiO_2$ thin films have been synthesized by the thermal treatment of a P123−$TiO_2$ mesophase hybrid. One can preferentially control the sintering temperature to preserve the mesostructure and allow for the sufficient crystallization of the framework wall. The resulting highly ordered mesoporous thin films have large surface areas and extended band gap energies. These 3D interconnected pore-wall systems show much higher photocatalytic activity than the conventional $TiO_2$ films. These results illustrate the potential of the zeolite-like mesoporous $TiO_2$ nanocrystalline thin films as an effective photocatalytic material. Their high light-harvesting capability, uniform mesopore arrays, and ease of surface modifications would also be useful for developing novel $TiO_2$-based optical/electronic materials.

**Acknowledgment.** The work described in this paper was financially supported by the Innovation and Technology Fund (ITS/118/01) and a grant from the Research Grants Council of the Hong Kong Special Administrative Region China (CUHK 4027/02P). This work was also partially supported by the National Natural Science Foundation of China (No. 20133010). The authors would like to thank Mr. T. K. Cheung for the TEM measurements and helpful discussions.

**Supporting Information Available:** Figures showing the low-angle XRD of the $TiO_2$ films, $N_2$ adsorption−desorption isotherms and BJH pore size distributions of the $TiO_2$ films, and HRSEM images of the mesoporous $TiO_2$ thin films (PDF). This material is available free of charge via the Internet at http://pubs.acs.org.

CM049955X

(22) Rolison, D. R. *Science* **2003**, *299*, 1698.

(23) (a) Corma, A. *Chem. Rev.* **1997**, *97*, 2373. (b) Pauly, T. R.; Liu, Y.; Pinnavaia, T. J.; Billinge, S. J. L.; Rieker, T. P. *J. Am. Chem. Soc.* **1999**, *121*, 8835.